

Ammonium Transporters Achieve Charge Transfer by Fragmenting Their Substrate

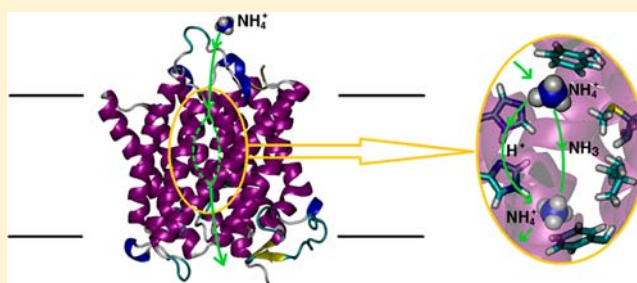
Shihao Wang,[†] Esam A. Orabi,[†] Sefer Baday,[‡] Simon Bernèche,^{*,‡} and Guillaume Lamoureux^{*,†}

[†]Department of Chemistry and Biochemistry and Centre for Research in Molecular Modeling (CERMM), Concordia University, 7141 Sherbrooke Street West, Montréal, Québec H4B 1R6, Canada

[‡]Swiss Institute of Bioinformatics and Biozentrum, University of Basel, Klingelbergstrasse 50/70, CH-4056 Basel, Switzerland

S Supporting Information

ABSTRACT: Proteins of the Amt/MEP family facilitate ammonium transport across the membranes of plants, fungi, and bacteria and are essential for growth in nitrogen-poor environments. Some are known to facilitate the diffusion of the neutral NH_3 , while others, notably in plants, transport the positively charged NH_4^+ . On the basis of the structural data for AmtB from *Escherichia coli*, we illustrate the mechanism by which proteins from the Amt family can sustain electrogenic transport. Free energy calculations show that NH_4^+ is stable in the AmtB pore, reaching a binding site from which it can spontaneously transfer a proton to a pore-lining histidine residue (His168). The substrate diffuses down the pore in the form of NH_3 , while the excess proton is cotransported through a highly conserved hydrogen-bonded His168–His318 pair. This constitutes a novel permeation mechanism that confers to the histidine dyad an essential mechanistic role that was so far unknown.



INTRODUCTION

Ammonium transport proteins have been found in all domains of life, notably in plants,¹ bacteria,² and mammals.^{3,4} They facilitate the membrane transport of ammonium (NH_4^+ and/or NH_3), which is an important nitrogen source for organisms such as bacteria, fungi, and plants,^{1,5} but a toxic metabolic waste product for others, such as mammals.^{4,6} The X-ray structures of bacterial ammonium transporter AmtB^{7–12} show a permeation pathway consisting of three regions (Figure 1a): a periplasmic vestibule, at the bottom of which is a binding site (S1) involved in ammonium recruitment; a gate formed of two phenylalanine residues (Phe107 and Phe215), whose function has not been fully established yet; and a narrow and hydrophobic pore lined with two hydrogen-bonded histidine residues (His168 and His318), in which various binding sites have been crystallographically identified.^{8,10–12} In the present work, we call “S2” the site where a substrate forms a hydrogen bond with His168 and “S4” the site where it forms a hydrogen bond with His318. The region between S2 and S4 is indistinctly called “S3”.

The recruitment of NH_4^+ in the periplasmic vestibule has been confirmed by structural and functional studies^{9,11,12} and by simulations.^{13–19} Under physiological pH, ammonium exists predominantly in its ionic form (NH_4^+), and the electron density maximum observed in the periplasmic vestibule of the AmtB channel is consistent with an ion forming cation– π interactions with aromatic amino acids Phe107 and Trp148, and an H-bond to Ser219. The identity of the transported species and the mechanism of transport have, however, not been confirmed so far. Because H_2O , NH_3 , and NH_4^+ are

isoelectronic molecules, they cannot be distinguished in the X-ray structures, and their assignment to electron density maxima remains hypothetical. In that regard, computer simulations based on quantum chemistry are an invaluable tool to investigate the affinity of the protein for the different forms of the substrate and the underlying transport mechanisms.

On the basis of experimental studies of various proteins of the Amt family, three transport mechanisms have been suggested: electroneutral NH_3 transport,^{9,11,12,14,16–18,20,21} NH_3/H^+ cotransport,^{9,22,23} and NH_4^+ transport.^{1,2,5,24,25} Despite this seemingly contradictory evidence, most theoretical studies^{13,15,19,26–28} have focused on electroneutral NH_3 transport mechanisms, in which NH_4^+ deprotonates in the periplasmic vestibule and a neutral NH_3 permeates through the pore, leaving the charge on the periplasmic side. This mechanism, however, leaves many experimental results unexplained.^{9,10,25} Electrophysiological studies of plant Amt²⁵ have confirmed a net charge transport across the membrane, which suggests that the transported substrate is either NH_4^+ or NH_3/H^+ . While the NH_3/H^+ cotransport hypothesis has been raised by many authors,^{22,29} it has not been demonstrated from a mechanistic perspective. Using computational methods based on quantum chemistry and statistical mechanics, we elucidate the pathway allowing for the binding of NH_4^+ and its subsequent splitting into NH_3 and H^+ . Our findings notably

Received: January 5, 2012

Published: May 25, 2012

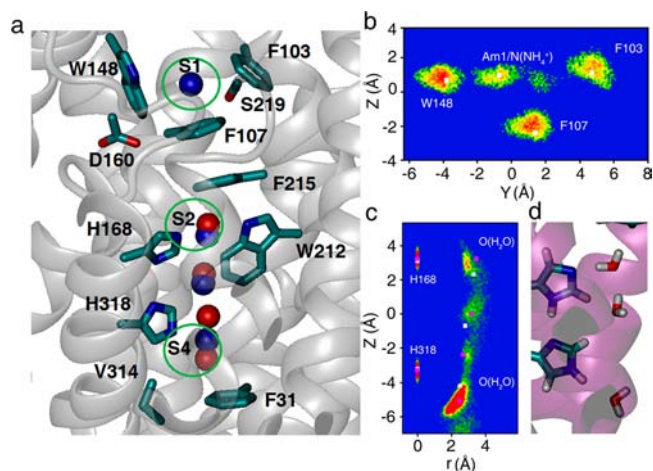


Figure 1. (a) Crystal structure of AmtB monomer (PDB id: 1U7G).¹¹ The locations of four density maxima identified by Khademi et al.¹¹ are marked as blue spheres. For comparison, four density maxima identified by Winkler et al. (PDB id: 1XQF, personal communication)¹² are marked as red spheres. Sites S1, S2, and S4 are depicted as green circles. Distribution of (b) NH_4^+ in site S1 and of (c) water in the AmtB pore, from 60 ns PM/MM simulations. In panel (b), positions are projected onto YZ plane and the distributions of ammonium nitrogen and centers of mass of F103, F107, and W148 rings are shown. In panel (c), positions are represented in cylindrical coordinates, using the N_ϵ atoms of His168 and His318 as principal axis. Distributions of water oxygen and N_ϵ atoms of His168 and His318 are shown. The density maxima from 1U7G and 1XQF crystal structures are shown as white and purple dots, respectively. A representative snapshot is shown in panel (d).

show that Amt's signature histidines are central for proton transport.

RESULTS AND DISCUSSION

Recruitment of NH_4^+ in Site S1. The stability of NH_4^+ in S1 was investigated using five independent 2 ns hybrid polarizable mechanics/molecular mechanics (PM/MM) simulations. Residues around site S1 are represented by polarizable models specifically parametrized to reproduce the complexation energies between NH_4^+ and a series of model compounds that represent protein side chains (see the Supporting Information, Figures S1,S2 and Tables S1,S2). NH_4^+ remains stable in site S1 along all simulations, at a position in agreement with site Am1 from the crystal structure of Khademi et al.¹¹ (Figure 1b), and in line with simulations from other groups.^{15,19,23} NH_4^+ forms a cation- π interaction with Trp148 most of the time, but it occasionally separates to form a cation- π interaction with

Phe103 (Figure 1b). The average distances from NH_4^+ to Ser219, Phe107, Phe103, Trp148, and H-bonding water are 2.8, 3.7, 5.9, 4.2, and 2.8 Å, respectively (see Table S3). During the simulations, the so-called hydrophobic pore is filled with water molecules, at positions in excellent agreement with the density observed in the 1U7G and 1XQF crystal structures (Figure 1c). This is consistent with our previous findings³⁰ and suggests that the pore in the crystal structures is occupied by water. While this conclusion appears to be somewhat force-field dependent,^{13,16,30} there is little doubt that the electronic density observed in the 1XQF structure is due to water, because the protein was crystallized in the absence of ammonium salt.¹²

Binding affinity of NH_4^+ for S1 is calculated from the free energy associated with the $\text{H}_2\text{O} \rightarrow \text{NH}_4^+$ alchemical transformation³¹ in the binding site, relative to the free energy associated with the same transformation in liquid water. The free energy difference represents the thermodynamic cost of exchanging an ammonium ion in the periplasm with a water molecule in the binding site. As shown in Table 1, the NH_4^+ binding affinity in S1 is -14.1 ± 1.5 kcal/mol, corresponding to a dissociation constant of 2.56 nM. By comparison, Luzhkov et al.,¹⁶ using a conventional (nonpolarizable) force field, have calculated $\Delta\Delta G_{\text{bind}}(\text{H}_2\text{O} \rightarrow \text{NH}_4^+)$ in S1 to be -5.8 kcal/mol, corresponding to a dissociation constant of 3.1 mM. This millimolar affinity is too low to explain the observed activity of Amt proteins, because *E. coli* can grow normally without a functional AmtB protein down to ammonium concentrations of $\sim 0.1 \mu\text{M}$,²¹ and because AmtB is actually being inactivated for ammonium concentrations greater than $\sim 5\text{--}50 \mu\text{M}$.³² The nanomolar affinity of S1 for ammonium ions is consistent with that of known benzene-based, synthetic receptors. For instance, Ahn et al.³³ have synthesized a tripodal oxazoline receptor that binds NH_4^+ with an affinity of 40 nM ($K_a = 2.5 \times 10^7 \text{ M}^{-1}$) and a free energy of -12.5 kcal/mol.

The high binding affinity in S1 is partially due to cation- π interactions resulting from the direct coordination of NH_4^+ with Phe107 and Trp148. A number of computational investigations have shown that, in aqueous solution, NH_4^+ - π interactions are significantly stronger than NH_4^+ -water interactions.³⁴⁻³⁶ For instance, Gallivan and Dougherty³⁵ have estimated the binding free energy of a methylammonium-benzene pair in solution to be -5.5 kcal/mol (as compared to -2.2 kcal/mol for a methylammonium-acetate pair). Sa et al.³⁶ have performed Car-Parrinello molecular dynamics simulations of an ammonium-benzene pair in aqueous solution and estimated the "cation- π " binding free energy to be -5.75 kcal/mol.

Table 1. Relative Binding Free Energies of NH_4^+ , Na^+ , and K^+ at the S1, S2, and S4 Sites (in kcal/mol)

mutation (site)	$\Delta G_{\text{mut}}^{\text{prot}}$	$\Delta G_{\text{mut}}^{\text{wat}}$	$\Delta\Delta G_{\text{bind}}$	K_d (nM) ^b
$\text{H}_2\text{O} \rightarrow \text{NH}_4^+$ (S1)	-75.8 ± 1.3^a	$-61.7 \pm 0.8^{a,c}$	-14.1 ± 1.5	2.56
$\text{H}_2\text{O} \rightarrow \text{NH}_4^+$ (S2)	-74.7 ± 0.6^a	$-61.7 \pm 0.8^{a,c}$	-13.0 ± 1.0	16.4
$\text{H}_2\text{O} \rightarrow \text{NH}_4^+$ (S4)	-70.3 ± 1.1^a	$-61.7 \pm 0.8^{a,c}$	-8.6 ± 1.4	2.75×10^4
$\text{H}_2\text{O} \rightarrow \text{Na}^+$ (S1)	-85.2	-80.3^d	-4.9	1.42×10^7
$\text{H}_2\text{O} \rightarrow \text{K}^+$ (S1)	-68.8	-62.9^e	-5.9	2.62×10^6

^aErrors are standard deviations from five independent simulations. ^bEquivalent dissociation constant calculated from $[W] \cdot \exp(\Delta\Delta G_{\text{bind}}/k_B T)$, where $[W]$ is the concentration of water (55.4 M) and k_B is the Boltzmann constant. ^cExperimental value is $-68.1 - (-6.32) = -61.8$ kcal/mol (using -6.32 kcal/mol as the experimental hydration free energy of water).^{77,78} Unlike solvation free energies, the calculated ΔG values do not contain the contribution from crossing the air-water interface (-12.6 kcal/mol for the SWM4-NDP model).^{68,79} ^dExperimental value is $-87.2 - (-6.32) = -80.9$ kcal/mol. ^eExperimental value is $-70.5 - (-6.32) = -64.2$ kcal/mol.⁷⁸

Experimental studies on AmtB⁹ and other Amt proteins^{1,25} have shown that site S1 is selective for NH₄⁺ over biologically abundant cations Na⁺ and K⁺. These ions do not permeate the proteins and do not even inhibit their ammonium-transport activity.^{1,9,25,37} We have calculated the binding free energies of Na⁺ and K⁺ from the free energies associated with the NH₄⁺ → Na⁺ and NH₄⁺ → K⁺ transformations, using a polarizable force field for all three ions (see the Supporting Information). As compared to NH₄⁺, the resulting binding affinities are reduced by 9.2 kcal/mol for Na⁺ and 8.2 kcal/mol for K⁺ (Table 1), which confirms that none of these ions would inhibit ammonium binding at physiological concentrations. The high selectivity of site S1 for NH₄⁺ is due to the specific coordination environment composed of the aromatic rings of Phe107 and Trp148, the hydroxyl group of Ser219, and two water molecules. While the number of coordinating ligands in S1 is comparable to that of NH₄⁺ in solution (4–5 water molecules²²), it is lower than that of Na⁺ or K⁺ (5–6 for sodium and 6–7 for potassium³⁸).

Affinity of NH₄⁺ in Site S2. We have investigated the probability of NH₄⁺ reaching the S2 binding site, which is separated from S1 by the two phenyl rings of Phe107 and Phe215. An ion bound to site S2 would be coordinated by residues Phe215, Trp212, and His168. Most of these residues are conserved throughout the Amt/MEP family,^{11,12} and mutagenesis studies on AmtB have shown that mutants F215A, W212A, and H168A are all inactive.^{9,10} Interestingly, mutant W212F, which preserves the aromatic character of the residue and therefore its ability to form a cation–π interaction with a charged substrate in S2, remains 80% active.⁹ This observation, along with the fact that Trp212 is conserved either as Trp or as Phe in all members of the Amt/MEP family, is suggesting that S2 is a cation-binding site and that tight ion-protein coordination in S2 is essential for transport.

The stability of NH₄⁺ at site S2 was investigated using two methods: PM/MM simulations as for site S1 and hybrid quantum mechanics/molecular mechanics (QM/MM) simulations. NH₄⁺ is initially placed at S2 and allowed to move freely, and the section of the pore below S2 is filled with water. The His168–His318 pair has two tautomers, depending on which of the two histidines is the hydrogen-bond donor to the other. The “His168–H···His318–H” structure (see Figure 1d) is considered to be the functional state at the time the substrate reaches S2. The reverse “H–His168···H–His318” state, which has a hydrogen atom pointing toward S2, would create an unfavorable electrostatic clash with NH₄⁺ in S2. The distributions of NH₄⁺ and water molecules in the pore are presented in Figure 2a and b. NH₄⁺ maintains a strong hydrogen bond to His168 throughout both the 4 ns PM/MM simulation and the 60 ps QM/MM simulation. According to the PM/MM simulations, the average distances from NH₄⁺ to His168, Phe215, Trp148, and H-bonding water are 3.0, 3.2, 3.2, and 3.0 Å, respectively. The positions of ammonium, water, and His168 are represented by nitrogen, oxygen, and Ne, respectively. For Phe215 and Trp148, the positions are represented by the center of their six-membered rings. Although NH₄⁺ is stable in S2, and favors the formation of a highly structured water chain in the pore (Figure 2a), its position does not correspond to any of the density maxima identified from X-ray crystallography, which are likely to represent water in a substrate-free pore (see Figure 1c).

The position of NH₄⁺ is more diffuse for the QM/MM simulations (Figure 2b), because they allow NH₄⁺ to

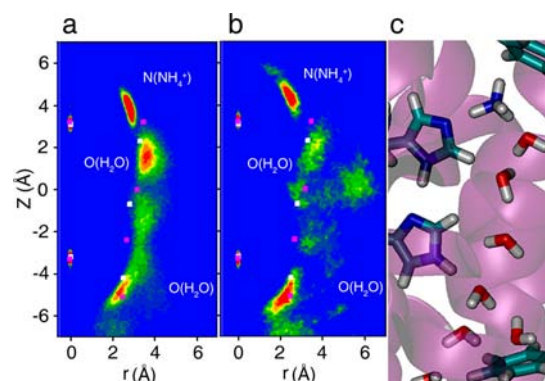


Figure 2. Distribution of NH₄⁺ in S2 and of water in the pore, from (a) 4 ns PM/MM simulations and (b) 60 ps QM/MM simulations. Positions are represented as in Figure 1c. Distributions of ammonium nitrogen, water oxygen, and Ne atoms of His168 and His318 are shown. For reference, the density maxima from 1U7G and 1XQF crystal structures are shown as white and purple dots, respectively. Panel (c) illustrates a representative configuration of the molecules.

deprotonate and represent a mixture of two states: an NH₄⁺ ion bound to a neutral His168 and an NH₃ molecule bound to a protonated His168. The water molecules are more dynamic as well, showing a binding pattern extending away from the histidine scaffold. Free QM/MM simulations with methylammonium (CH₃NH₃⁺, also known to permeate¹¹) in S2 yield distributions similar to those of Figure 2b, also involving proton transfer between CH₃NH₃⁺ and His168.

As reported in Table 1, the calculated NH₄⁺ binding affinity in site S2 is -13.0 ± 1.0 kcal/mol, which indicates that NH₄⁺ is almost as stable in S2 as it is in S1. This large binding free energy is consistent with mutagenesis data^{9,39} showing that AmtB retains its activity even for a highly disrupted S1 site. The high ammonium affinity of S2 would explain why the triple mutant F107A/W148A/S219A (in which the Phe, Trp, and Ser residues around S1 are mutated to alanine) is even more active than the wild-type protein.⁹ In stark contrast, Luzhkov et al.¹⁶ report a free energy barrier of +22.1 kcal/mol when the pore is filled with ammonia instead of water, using a conventional nonpolarizable force field.

It is expected that the translocation of NH₄⁺ from S1 to S2 requires a transient reorganization of the aromatic side chains of Phe107 and Phe215. In accordance with a number of simulation studies,^{13,15,18} our simulations show that the side chains of Phe107 and Phe215 frequently rotate and adopt conformations in which the two aromatic rings are perpendicular and form an “L” shape susceptible to bind NH₄⁺ at an intermediate position between S1 and S2. An ammonium ion at that position would be stabilized by an H-bond with the Ala162 backbone, which would significantly reduce the translocation energy barrier. Mutagenesis data from Javelle et al.⁹ show that F107A variant remains active but that variant F215A and double variant F107A/F215A are inactive, yet that none of these mutants leak water. This suggests that the phenylalanine gate is not so much preventing water from diffusing as it is providing key residues leading the substrate to S2 and stabilizing it in the vicinity of His168. Given the binding free energies of NH₄⁺ at S1 and S2 (-14.1 and -13.0 kcal/mol, respectively), the probability of the substrate going to S2 is much greater than the probability of it going back to the periplasm, irrespective of the details of the translocation mechanism.

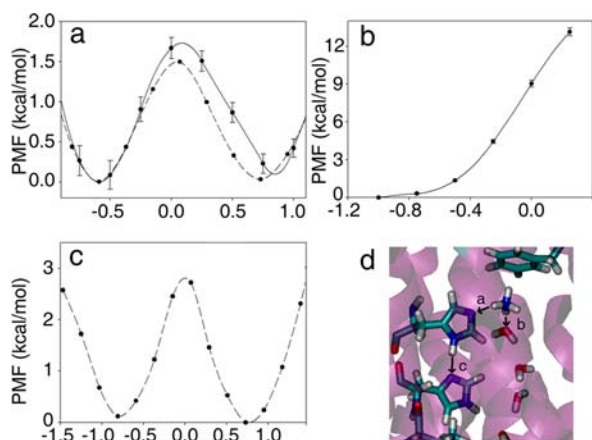


Figure 3. Potentials of mean force (PMFs) for proton transfer reactions involving ammonium in site S2: (a) from ammonium to His168, (b) from ammonium to pore water, and (c) from His168 to His318. Panel (d) illustrates the proton transfer reactions, and the arrows correspond to the reaction from left to right in each panel. The results from constrained and unconstrained QM/MM simulations are shown in solid and dashed lines, respectively. Reaction coordinates are defined as: $RC = d_{N(\text{amm})-H} - d_{N\epsilon(\text{His168})-H}$ for panel (a), $RC = d_{N(\text{amm})-H} - d_{O(\text{wat})-H}$ for panel (b), and $RC = d_{N\delta(\text{His168})-H} - d_{N\delta(\text{His318})-H}$ for panel (c). Note the different energy scales in panels (a)–(c). Error bars in panels (a) and (b) are calculated from the block averaging of mean forces.⁷⁶

Mechanism of NH_4^+ Deprotonation in S2. We investigated two mechanisms for ammonium deprotonation at S2: (1) through the histidine side chains and (2) through the water chain in the pore (Figure 3). Water chains are common proton pathways in proteins and in nanotubes^{40–44} but are most effective when water molecules are the only available proton acceptors. In the presence of a better proton acceptor, such as ammonia or the unsaturated nitrogen atom of a histidine side chain, the proton conductivity of the chain may be significantly reduced.^{45,46} Imidazole, a model compound for the histidine side chain, has a higher proton affinity than water (225.2 kcal/mol versus 165.1 kcal/mol for water⁴⁷) and a higher basicity (7.0 versus -1.74).

The two deprotonation mechanisms are analyzed by calculating the potentials of mean force (PMFs) of proton transfer using constrained QM/MM simulations. The free energy barrier for the proton transfer from NH_4^+ to His168 is only 1.7 kcal/mol, and the two protonation states are almost equally stable (Figure 3a). In contrast, proton transfer from NH_4^+ to the adjacent water molecule is prohibited (Figure 3b). As the excess proton is pushed toward the water molecule, forming an H_3O^+ ion, the system becomes chemically unstable, and another proton is quickly transferred from H_3O^+ to NH_3 .

This finding is consistent with the unconstrained QM/MM simulations of NH_4^+ in S2. In these simulations, proton transfer between NH_4^+ and His168 happens about 40 times in 60 ps. Proton transfer between His168 and His318 is also observed (8 times in 60 ps), indicating that NH_4^+ , His168, and His318 form a charge-delocalized structure⁴¹ that entropically stabilizes the excess positive charge. The distribution of protons from the unconstrained simulations is converted into proton transfer PMFs using the equation:

$$W(X) = -k_B T \ln \rho(X)$$

where $\rho(X)$ is the distribution of reaction coordinate X and $W(X)$ is the corresponding PMF (see dashed lines in Figure 3a and c). Proton transfer events between NH_4^+ and His168 are frequent enough that the unconstrained QM/MM PMF is statistically converged. The energy barrier for the proton transfer between His168 and His318 is 2.8 kcal/mol (Figure 3c), which is higher than that for the transfer between NH_4^+ and His168 but is low enough to be sampled at the picosecond time scale. The two protonation states have the same free energy.

The deprotonation mechanism observed in the QM/MM simulations is consistent with ab initio energy profiles calculated for the proton transfer reactions from an ammonium ion to imidazole (representing His168) and from an ammonium ion to water (see Figure S4a). On the basis of comparisons with ab initio calculations performed in various implicit solvents, it appears that the protein environment of a histidine-bound ammonium in S2 has a polarity intermediate to that of liquid benzene and liquid water, such that the substrate exists both as NH_4^+ and as NH_3 bound to a protonated histidine.

The QM/MM simulations provide the following picture: As soon as NH_4^+ reaches site S2, the excess proton delocalizes in three tautomeric forms, $\text{NH}_4^+ \cdots \text{His168} \cdots \text{His318}$, $\text{NH}_3 \cdots \text{His168H}^+ \cdots \text{His318}$, and $\text{NH}_3 \cdots \text{His168} \cdots \text{His318H}^+$. The three forms are almost iso-energetic and exchange on the picosecond time scale: on average every ~ 1.5 ps between ammonia and His168 and every ~ 7.5 ps between His168 and His318. This charge-delocalized structure stabilizes the excess proton and may further increase the NH_4^+ affinity of the S2 binding site.

These findings suggest that the His168–His318 dyad, which is highly conserved among proteins of the Amt/MEP family, is essential for ammonium binding and deprotonation. This is consistent with the fact that mutants H168A, H168F, H318A, and H318F are all inactive,¹⁰ as none of these variants can H-bond to NH_4^+ and serve as general base for deprotonation. The H168E mutant, on the other hand, retains 25% of the wild-type activity,^{10,39} consistent with the fact that the two side chains have similar basicities (9.2 for acetic acid, versus 7.0 for imidazole) and can form an H-bond with residue His318. We have performed two independent 30 ps unconstrained QM/MM simulations of the H168E mutant (where His168 is replaced by a neutral Glu, acting as H-bond donor to His318), which display a similar deprotonation process and fast proton movement across $\text{NH}_4^+ \cdots \text{Glu168} \cdots \text{His318}$. This indicates that the deprotonation mechanism is robust and could be operating in fungal homologues having a Glu residue at position 168.⁴⁸

NH_3 Diffusion along the Protonated His168–His318 Dyad. The leaving of NH_3 from S2 creates a more confined charge-delocalized structure that has only two protonation states: $\text{His168H}^+ \cdots \text{His318}$ and $\text{His168} \cdots \text{His318H}^+$. These two states are almost equally populated (Figure 3c), and alternate at a rate faster than the substrate diffusion process. The proton transfer between His168 and His318 has a time scale of ~ 7.5 ps, but not a single NH_3 translocation event was observed in 60 ps of unconstrained QM/MM simulations. The NH_3 substrate diffusing down the pore is therefore experiencing the field created by a mixture of both protonation states.

PMFs of NH_3 diffusion are calculated using the adaptive biasing force (ABF) method for both the “His168H⁺” and the “His318H⁺” states (Figure 4). The two states give slightly different free energy profiles, but both display low energy

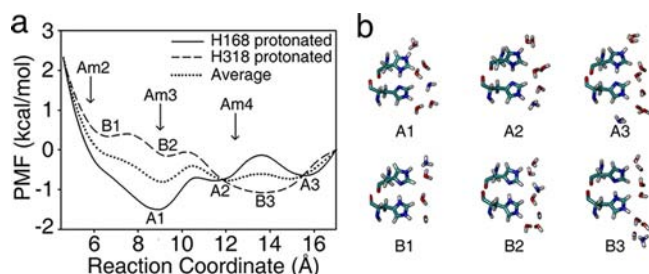


Figure 4. PMFs for NH_3 permeation after deprotonation at site S2. Two protonation states of the histidine side chains are considered: “His168 protonated” (solid-line PMF, snapshots A1–A3) and “His318 protonated” (dashed-line PMF, snapshots B1–B3). The reaction coordinate is the z -coordinate offset of ammonia from the center of the Phe107 ring. The positions of sites Am2, Am3, and Am4 are from structure 1U7G.¹¹

barriers to NH_3 diffusion. The average PMF, representing the force actually experienced by the substrate, is shown as a dotted line in Figure 4a. Note that in its neutral NH_3 form, the substrate is more likely to leave site S2 by exchanging with a water molecule in the pore than recrossing the Phe107/Phe215 gate (Figure 4a). The overall diffusion process is essentially barrierless.

Reprotonation of NH_3 at Site S4. The excess proton is most likely to remain bound to the histidine side chains as long as sites S2 and S4 are occupied by water molecules, which are poor acceptors for the histidine protons (Figure S4d). However, as soon as NH_3 reaches S4, the excess proton has a much higher probability of transfer. NH_3 is more exposed to solvent in site S4 than in site S2. The ABF simulations show that NH_3 is usually coordinated by one water molecule in S2 but by 2 to 3 water molecules in S4. This increase in polarity of the environment stabilizes the $\text{His318}\cdots\text{NH}_4^+$ form over the $\text{His318H}^+\cdots\text{NH}_3$ one (Figure S4a).

We investigated the reprotonation of NH_3 in S4 using two independent 30 ps unconstrained QM/MM simulations, in which NH_3 is initially placed at the hydrogen-bonding position from His318 and is allowed to move freely. The substrate is most likely found at this position (Figure 5c), but it

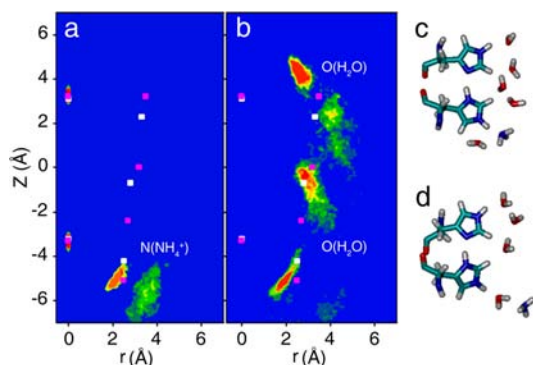


Figure 5. Distribution of $\text{NH}_3/\text{NH}_4^+$ near site S4 from 60 ps QM/MM simulations. Panel (a) shows the distribution of $\text{NH}_3/\text{NH}_4^+$, and panel (b) shows the distribution of water. Positions are represented as in Figure 1c. For reference, the density maxima from 1U7G and 1XQF crystal structures are shown as white and purple dots, respectively. Panel (c) is showing NH_3 hydrogen bonding to His318, and panel (d) is showing NH_3 indirectly hydrogen bonding to His318 (through water).

occasionally moves away and binds His318 through a water molecule (Figure 5d). This corresponds to the secondary density maximum of Figure 5a, at $Z \approx -6$ Å. During the QM/MM simulations, proton transfer is observed for NH_3 at both positions, directly or through a water bridge (Figure S5). In both cases, the substrate remains in contact with the aromatic ring of Phe31, which may provide a stabilizing cation– π interaction for NH_4^+ on its way to the cytoplasm. The reprotonation of NH_3 was further analyzed using constrained QM/MM simulations. The free energy barrier for the proton transfer from His318 to NH_3 is 2.5 kcal/mol, and the free energy of reaction is 1.3 kcal/mol (Figure S4e).

As reported in Table 1, the calculated NH_4^+ binding affinity in site S4 is -8.6 ± 1.4 kcal/mol, corresponding to a dissociation constant of 2–290 μM . Considering that the internal NH_4^+ concentration is expected to be lower than the micromolar³² (or even submicromolar²¹) extracellular concentration, this suggests that the average substrate occupancy of S4 is significantly lower than that of S1/S2.

Coupling between NH_3 and H^+ Transport. While protonation states $\text{His168H}^+\cdots\text{His318}$ and $\text{His168}\cdots\text{His318H}^+$ are almost equally populated when the substrate occupies site S2 (see Figure 3c), independent QM/MM simulations show that the “His318 protonated” state becomes increasingly stable as the substrate diffuses down the pore as NH_3 , from S2 to S4 (Figure S4c). Therefore, the excess proton will likely be on His318 when the substrate reaches the lower section of the pore, in position to be reprotonated. While this suggests that the transport of NH_3 and H^+ is concerted, it is worth noting that any small molecule from the cytoplasm reaching S4 before NH_3 (such as HCO_3^- or HPO_4^{2-}) could take the proton without disrupting the $\text{NH}_3:\text{H}^+$ transport stoichiometry. It is unlikely that the excess proton stored in the histidine dyad will be shuttled back to the periplasm after the departure of NH_3 from S2, because there is no residue above His168 that can act as proton acceptor, and because the Phe107/Phe215 gate precludes the formation of a proton wire between S2 and S1. The transport of NH_3 and H^+ therefore appears to be coupled in a 1:1 stoichiometry.

Reset of His168 and His318 Protonation States. Each cotransport of a proton through the His168–His318 dyad takes the system from a “His168–H \cdots His318–H” state, required for substrate deprotonation in S2, to a “H–His168 \cdots H–His318” state, that cannot bind NH_4^+ in S2 and is essentially inactive for NH_3/H^+ cotransport. For the transport cycle to repeat, the original protonation state of the histidines has to be restored.

We have investigated a “reset” mechanism based on the formation of a transient water chain in the pore that creates a cyclic hydrogen-bond network formed of two histidines and four or five water molecules between S2 and S4. Such transient conformation has been observed repeatedly in our free simulations of the “H–His168 \cdots H–His318” state. Once that cyclic proton wire (or “proton loop”) is formed, two opposite reaction pathways can be imagined: (1) a “hydronium” pathway, in which the proton from $\text{N}\epsilon$ of His168 is transferred to the top water molecule in the pore, forming an unstable H_3O^+ ion that diffuses down the water chain according to a Grotthuss-like mechanism and transfers its excess proton to $\text{N}\epsilon$ of His318; and (2) a “hydroxide” pathway, in which $\text{N}\epsilon$ of His318 gets a proton from water, generating an OH^- ion that diffuses up and receives the excess proton from $\text{N}\epsilon$ of His168.

On the basis of gas-phase ab initio calculations (Figure S6a–c), the “hydroxide” pathway has a much lower energy barrier

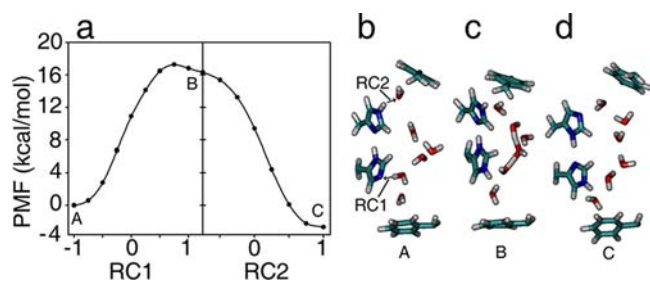


Figure 6. PMFs for proton transfer between His168 and His318 through a water chain calculated from QM/MM simulations in the protein environment. Panel (a) shows the free energy profile along two reaction coordinates, which are defined as $RC1 = d_{O(\text{water in } S4)-H} - d_{N(\text{His318})-H}$ and $RC2 = d_{N(\text{His168})-H} - d_{O(\text{water in } S2)-H}$. Panels (b), (c), and (d) are snapshots for reactant A, intermediate B, and product C, respectively. The reaction coordinates are illustrated in panel (b). When RC1 is scanned, RC2 is fixed at 0.75 Å, and when RC2 is scanned, RC1 is fixed at 1.25 Å. Each point corresponds to a 5 ps constrained QM/MM simulation.

than the “hydronium” pathway and is strongly favored. The detailed mechanism was investigated using constrained QM/MM simulations with five water molecules between S2 and S4. The free energy surface along the “hydroxide” pathway (Figure 6a) shows an activation energy of 17.2 ± 0.5 kcal/mol and a shoulder corresponding to an OH^- ion coordinated by three water molecules (Figure 6c). Although four water molecules between S2 and S4 are sufficient to create a stable proton loop, the additional water molecule creates a full hydration shell around the hydroxide anion⁴⁹ and results in a significantly lower free energy barrier (Figure S6d). Although the reaction

barrier is relatively high, similar or even higher barriers have been seen in many proton transfer processes in proteins.^{50–52}

This “hydroxide” pathway is analogous to the “proton hole” mechanism proposed by Riccardi et al.⁵³ for a proton transfer between two imidazole moieties in solution. The “hole” is the deprotonated state of any mediating molecule⁵³ and, in the AmtB system, is transferred from His318 to His168 through bridging water molecules. We have also considered other resetting mechanisms, but they all happen to be less likely. For instance, the His168 and His318 rings may rotate to be parallel or flip around to facilitate proton transfer. However, our calculations have shown that the rotation of the rings alone (before any proton transfer) has a free energy cost greater than 20 kcal/mol and results in no stable product state.

To directly estimate the relative free energies of the “H–His168···H–His318” and “His168–H···His318–H” states, we have used PM/MM simulations to calculate the mutation free energy from one state to the other. The resulting free energy is $+1.7 \pm 0.8$ kcal/mol, as compared to +3.5 and –2.6 kcal/mol from the QM/MM simulations, depending on the specific structure of the water chain (see Figure S6). This confirms that the two His–His protonation states have comparable energies once the water molecules in the pore adopt their equilibrium configuration.

This reset step is likely to have slow kinetics and is possibly the rate-determining step in the transport process. The experimental transport rate under nitrogen-limiting conditions is 10–10 000 molecules per second,¹² which can be converted to an overall activation energy of 12.5–16.6 kcal/mol, using Eyring’s rate theory with a prefactor of $1.5 \times 10^{13} \text{ s}^{-1}$ derived from our simulations of the proton transfer reaction between

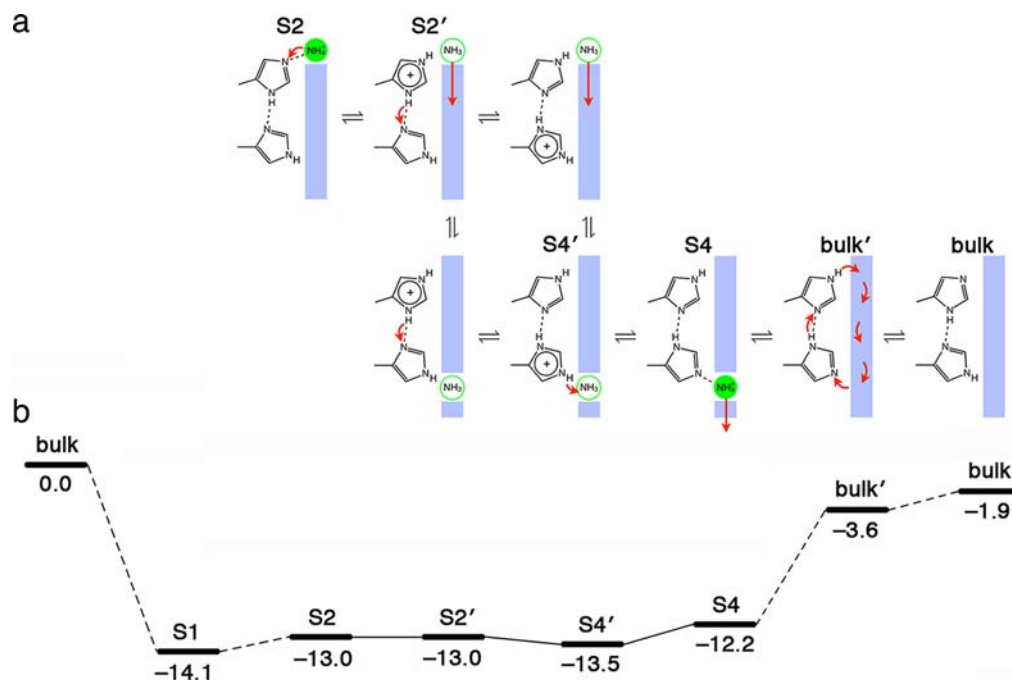


Figure 7. Schematic illustration of the NH_3/H^+ cotransport cycle. Panel (a) shows the scheme of the transport mechanism. Each state is labeled according to the positions of $\text{NH}_4^+/\text{NH}_3$ in the pore. NH_4^+ in site S2 transfers its excess proton to the His168–His318 dyad. After deprotonation, NH_3 can diffuse down the pore into S4 binding site, where it can receive the excess proton from His318. Once NH_4^+ moves out of the pore (state bulk'), the protonation state of the His168–His318 dyad is reset by a concerted proton transfer through a water chain in the pore. Areas in blue represent water-accessible regions. Curved red arrows represent proton transfer, and straight red arrows represent substrate diffusion. Panel (b) shows the free energies (in kcal/mol) of the most important structures in the transport process. The first and the last states are the same in the thermodynamic cycle.

His168 and His318 (see section Mechanism of NH_4^+ Deprotonation in S2). The calculated barrier of 17.2 ± 0.5 kcal/mol for the reset of the protonation state of His168 and His318 is slightly above that range, but considering that concerted proton transfer reactions usually show enhanced nuclear quantum effects,^{54,55} the effective barrier is expected to be 2–6 kcal/mol lower when zero-point energy and tunneling effect corrections are applied.^{56–58} The overall cotransport mechanism is therefore consistent with the experimental rate.

CONCLUSION

We have investigated cotransport mechanisms for net ammonium (NH_4^+) transport through AmtB using PM/MM, QM/MM simulations, and ab initio calculations. The overall mechanism is summarized in Figure 7a, and the free energy levels along the transport cycle are shown in Figure 7b. The free energy over the whole cycle is -1.9 kcal, which is an indication of the accuracy of our calculations. (In the absence of a trans-membrane potential, a perfectly sampled simulation, performed using a consistent description of the atomic forces, would result in a strictly zero free energy difference over the cycle.) Our simulations show that site S1 provides a coordination that is highly selective for NH_4^+ over Na^+ and K^+ ions. They also show that NH_4^+ is stable in site S2, where it is involved in two cation– π interactions (with Phe215 and Trp212) and two hydrogen bonds (with His168 and one of the water molecules in the pore). First-principles calculations show that, once NH_4^+ reaches S2, the excess proton easily transfers to His168 and the complex $\text{NH}_4^+\cdots\text{His168}\cdots\text{His318}$ forms a charge-delocalized structure in which rapid proton movement is observed. After deprotonation, NH_3 diffuses through the hydrophobic pore with almost no free energy barrier. Once it reaches site S4, the Phe31-coordinated substrate accepts a proton from His318H⁺ (either directly or through a bridging water molecule) and diffuses into the cytoplasm as NH_4^+ .

The deprotonation/diffusion/reprotonation of ammonium leaves the His168–His318 pair in a protonation state that is inactive for the next cotransport cycle. To restore the initial state, a proton needs to transfer from His168 to His318 through a chain of water molecules occupying the pore. This “histidine reset” mechanism involves a high-energy intermediate, as expected from the experimental turnover rate of AmtB, which is more in line with the rate of a conventional enzyme than of a channel. Contrary to other slow processes, such as the diffusion of NH_4^+ through the pore as a whole (which is kinetically irrelevant because NH_4^+ deprotonation in S2 is spontaneous), the “reset” step appears to be a kinetic bottleneck.

Because of the technical challenge of measuring slow transport events, it remains unclear whether AmtB favors the transport of NH_3 or NH_4^+ .⁹ Mutants F107A, W148A, and S219A are all more active than the wild-type protein.⁹ Even the triple mutant F107A/W148A/S219A, for which all residues coordinating the substrate in S1 are displaced, is slightly more active than the wild type.⁹ This clearly shows that S1 is not essential for the activity. According to most propositions of a neutral (NH_3) permeation mechanism, site S1 is important for the recruitment and deprotonation of NH_4^+ . None of these functions are likely to play out the same in the triple mutant. Furthermore, mutagenesis studies show that all residues surrounding site S2 are important for the activity.¹⁰ Mutants of F215, W212, and H168 are mostly inactive, with the exception of W212F and H168E. Both of these active mutants

are still functional in the NH_3/H^+ cotransport mechanism we are proposing.

The electrogenic mechanism presented here does not exclude that electroneutral transport might also take place. However, it illustrates the most plausible pathway for the transport of the charged NH_4^+ in the Amt/MEP family of proteins and highlights the role of the two histidines lining the pore. Our calculations also show that a glutamic acid residue in position 168 could play the same role, suggesting that *Saccharomyces cerevisiae*'s Mep1 and Mep2⁴⁸ (in which His168 is replaced by Glu) may also exploit this mechanism.

EXPERIMENTAL DETAILS

Simulation System Preparation. The AmtB monomer structure used in this work is based on the X-ray structure determined by Khademi et al.¹¹ (Protein Data Bank ID: 1U7G). Three mutated residues (F68S, S126P, and K255L) in 1U7G are modified back to their native states. Both His168 and His318 are neutral. We use the “His168–H \cdots His318–H” protonation state for the initial structure, based on our previous simulation study³⁰ showing that this state reproduces the experimental density¹² inside the pore much more accurately than the reverse “H–His168 \cdots H–His318” state. The Membrane Builder tool of CHARMM-GUI⁵⁹ is then used to add a lipid bilayer and a water box with dimensions of $92.3 \text{ \AA} \times 77.4 \text{ \AA} \times 91.2 \text{ \AA}$ around the monomer. Specifically, 185 dimyristoylphosphatidylcholine (DMPC) molecules (94 on the periplasmic side and 91 on the cytoplasmic side) and 13 111 TIP3P water molecules⁶⁰ are added, and the system is neutralized by adding 34 K^+ and 36 Cl^- ions, corresponding to 0.1 M salt concentration. All simulations are equilibrated for at least 200 ps before data collection.

Molecular Dynamic (MD) Simulations. MD simulations are performed with the CHARMM program,⁶¹ using a hybrid polarizable mechanics/molecular mechanics (PM/MM) description of the system. NH_4^+ and surrounding water molecules and protein side chains are described by a polarizable force field based on the classical Drude oscillator,^{62–65} and parametrized to reproduce both the free energy of hydration and the ion–protein interactions. The rest of the system is described by the nonpolarizable CHARMM param27 force field.⁶⁶ See the Supporting Information and Figure S3 for details.

Binding Free Energy Calculations. Relative binding free energies ($\Delta\Delta G_{\text{bind}}$) are calculated using the standard thermodynamic integration method,⁶⁷ as combinations of free energies of mutation of NH_4^+ to H_2O at S1, S2, S4, and in bulk water. Mutations are performed using a hybrid residue that corresponds to the NH_4^+ polarizable model when $\lambda = 0$ and to the SWM4 water model when $\lambda = 1$ (see Figure S3d). The transition of λ from 0 to 1 is split into 12 windows: 0, 0.05, 0.15, 0.25, 0.35, 0.45, 0.55, 0.65, 0.75, 0.85, 0.95, and 1. Each window corresponds to an independent simulation that includes 100 ps of equilibration and 100 ps of data collection. Five independent calculations are performed to get more reliable results and to estimate errors. The free energy calculations in the protein ($\Delta G_{\text{mut}}^{\text{prot}}$) use polarizable force fields as described in the previous section. Free energies of hydration ($\Delta G_{\text{mut}}^{\text{wat}}$) are calculated in a periodic system of 2000 SWM4 water molecules. The solvent box is large enough that the resulting solvation free energies show no system-size dependency. Because the system is periodic, the free energies do not contain a contribution from the air–water interface.⁶⁸

Quantum Mechanics/Molecular Mechanics (QM/MM) Simulations. QM/MM simulations are performed using the CP2K program.⁶⁹ The details of the CP2K setup can be found in the Supporting Information. All initial structures used in QM/MM simulations are equilibrated by PM/MM simulations for at least 1 ns. The QM region includes NH_4^+ , the surrounding side chains, and water molecules in the hydrophobic pore. The QM box is approximately $14 \text{ \AA} \times 18 \text{ \AA} \times 22 \text{ \AA}$, 6–8 \AA larger than the extent of the QM fragments in each direction.

Constrained QM/MM Simulations. Potentials of mean force (PMFs) of proton transfer reactions are calculated using constrained

QM/MM molecular dynamics simulations. The reaction coordinate for a proton transfer, X , is defined as the difference in distances from the proton to the two heavy atoms involved in the hydrogen bond. The range of X is divided into nine windows (-1 , -0.75 , -0.5 , -0.25 , 0 , 0.25 , 0.5 , 0.75 , and 1 Å), and individual QM/MM simulations are performed for each window with X fixed using a Lagrange multiplier. The constraint forces are collected and then integrated over the full range of X to generate the PMF.

Adaptive Biasing Force (ABF) Simulations. PMFs for NH_3 permeation in the hydrophobic pore are calculated using the ABF method,^{70–73} implemented in the NAMD program.⁷⁴ CHARMM param27 force field⁶⁶ is used for all residues and water, and OPLS model⁷⁵ is used for NH_3 . Two PMFs are calculated: one with charged His168 and neutral His318 and the other with neutral His168 and charged His318. The reaction coordinate is the Z -coordinate offset of NH_3 from the center of the phenyl ring of Phe107. NH_3 is forced to move within the range $\text{RC} = 4.5\text{--}17.0$ Å. For each PMF, the system is equilibrated for 1 ns, and data are collected for 30 ns.

■ ASSOCIATED CONTENT

● Supporting Information

Parameterization of polarizable force fields, simulation system setup, details of free energy calculations, and additional results. This material is available free of charge via the Internet at <http://pubs.acs.org>.

■ AUTHOR INFORMATION

Corresponding Author

guillaume.lamoureux@concordia.ca; simon.berneche@unibas.ch

Notes

The authors declare no competing financial interest.

■ ACKNOWLEDGMENTS

We thank Arnaud Javelle for discussions and critical reading of the manuscript. This work has been supported by an FQRNT Nouveaux chercheurs grant to G.L., by a grant from the Swiss National Science Foundation to S.B. (SNF-Professorship #118928), and by a PROTEO scholarship and a GEPROM scholarship to E.A.O. Computational resources were provided by Calcul Québec and by the Swiss National Supercomputing Centre (CSCS).

■ REFERENCES

- (1) Ninnemann, O.; Jauniaux, J. C.; Frommer, W. B. *EMBO J.* **1994**, *13*, 3464–3471.
- (2) Siewe, R. M.; Weil, B.; Burkovski, A.; Eikmanns, B. J.; Eikmanns, M.; Kramer, R. *J. Biol. Chem.* **1996**, *271*, 5398–5403.
- (3) Marini, A. M.; Matassi, G.; Raynal, V.; André, B.; Cartron, J. P.; Cherif-Zahar, B. *Nat. Genet.* **2000**, *26*, 341–344.
- (4) Marini, A. M.; Urrestarazu, A.; Beauwens, R.; André, B. *Trends Biochem. Sci.* **1997**, *22*, 460–461.
- (5) Marini, A. M.; Soussi-Boudekou, S.; Vissers, S.; André, B. *Mol. Cell. Biol.* **1997**, *17*, 4282–4293.
- (6) Marini, A. M.; Vissers, S.; Urrestarazu, A.; André, B. *EMBO J.* **1994**, *13*, 3456–3463.
- (7) Conroy, M. J.; Durand, A.; Lupo, D.; Li, X. D.; Bullough, P. A.; Winkler, F. K.; Merrick, M. *Proc. Natl. Acad. Sci. U.S.A.* **2007**, *104*, 1213–1218.
- (8) Gruswitz, F.; O'Connell, J.; Stroud, R. M. *Proc. Natl. Acad. Sci. U.S.A.* **2007**, *104*, 42–47.
- (9) Javelle, A.; Lupo, D.; Ripoché, P.; Fulford, T.; Merrick, M.; Winkler, F. K. *Proc. Natl. Acad. Sci. U.S.A.* **2008**, *105*, 5040–5045.
- (10) Javelle, A.; Lupo, D.; Zheng, L.; Li, X. D.; Winkler, F. K.; Merrick, M. *J. Biol. Chem.* **2006**, *281*, 39492–39498.
- (11) Khademi, S.; O'Connell, J.; Remis, J.; Robles-Colmenares, Y.; Miericke, L. J. W.; Stroud, R. M. *Science* **2004**, *305*, 1587–1594.
- (12) Zheng, L.; Kostrewa, D.; Bernèche, S.; Winkler, F. K.; Li, X. D. *Proc. Natl. Acad. Sci. U.S.A.* **2004**, *101*, 17090–17095.
- (13) Bostick, D. L.; Brooks, C. L. *PLoS Comput. Biol.* **2007**, *3*, 231–246.
- (14) Ishikita, H.; Knapp, E. W. *J. Am. Chem. Soc.* **2007**, *129*, 1210–1215.
- (15) Lin, Y. C.; Cao, Z. X.; Mo, Y. R. *J. Am. Chem. Soc.* **2006**, *128*, 10876–10884.
- (16) Luzhkov, V. B.; Almlöf, M.; Nervall, M.; Åqvist, J. *Biochemistry* **2006**, *45*, 10807–10814.
- (17) Nygaard, T. P.; Alfonso-Prieto, M.; Peters, G. H.; Jensen, M. O.; Rovira, C. *J. Phys. Chem. B* **2010**, *114*, 11859–11865.
- (18) Nygaard, T. P.; Rovira, C.; Peters, G. H.; Jensen, M. O. *Biophys. J.* **2006**, *91*, 4401–4412.
- (19) Akgun, U.; Khademi, S. *Proc. Natl. Acad. Sci. U.S.A.* **2011**, *108*, 3970–3975.
- (20) Soupene, E.; Chu, T.; Corbin, R. W.; Hunt, D. F.; Kustu, S. *J. Bacteriol.* **2002**, *184*, 3396–3400.
- (21) Soupene, E.; He, L. H.; Yan, D. L.; Kustu, S. *Proc. Natl. Acad. Sci. U.S.A.* **1998**, *95*, 7030–7034.
- (22) Boeckstaens, M.; André, B.; Marini, A. M. *J. Biol. Chem.* **2008**, *283*, 21362–21370.
- (23) Ludewig, U. *Transfusion Clin. Biol.* **2006**, *13*, 111–116.
- (24) Fong, R. N.; Kim, K. S.; Yoshihara, C.; Inwood, W. B.; Kustu, S. *Proc. Natl. Acad. Sci. U.S.A.* **2007**, *104*, 18706–18711.
- (25) Ludewig, U.; von Wirén, N.; Frommer, W. B. *J. Biol. Chem.* **2002**, *277*, 13548–13555.
- (26) Cao, Z.; Mo, Y.; Thiel, W. *Angew. Chem., Int. Ed.* **2007**, *46*, 6811–6815.
- (27) Lin, Y. C.; Cao, Z. X.; Mo, Y. R. *J. Phys. Chem. B* **2009**, *113*, 4922–4929.
- (28) Yang, H.; Xu, Y.; Zhu, W.; Chen, K.; Jiang, H. *Biophys. J.* **2007**, *92*, 877–885.
- (29) Lamoureux, G.; Javelle, A.; Baday, S.; Wang, S.; Bernèche, S. *Transfusion Clin. Biol.* **2010**, *17*, 168–175.
- (30) Lamoureux, G.; Klein, M. L.; Bernèche, S. *Biophys. J.* **2007**, *92*, L82–L84.
- (31) Straatsma, T. P.; McCammon, J. A. *Annu. Rev. Phys. Chem.* **1992**, *43*, 407–435.
- (32) Javelle, A.; Severi, E.; Thornton, J.; Merrick, M. *J. Biol. Chem.* **2004**, *279*, 8530–8538.
- (33) Ahn, K. H.; Ku, H. Y.; Kim, Y.; Kim, S. G.; Kim, Y. K.; Son, H. S.; Ku, J. K. *Org. Lett.* **2003**, *5*, 1419–1422.
- (34) Chipot, C.; Maigret, B.; Pearlman, D. A.; Kollman, P. A. *J. Am. Chem. Soc.* **1996**, *118*, 2998–3005.
- (35) Gallivan, J. P.; Dougherty, D. A. *J. Am. Chem. Soc.* **2000**, *122*, 870–874.
- (36) Sa, R. J.; Zhu, W. L.; Shen, J. H.; Gong, Z.; Cheng, J. G.; Chen, K. X.; Jiang, H. L. *J. Phys. Chem. B* **2006**, *110*, 5094–5098.
- (37) Bakouh, N.; Benjelloun, F.; Hulin, P.; Brouillard, F.; Edelman, A.; Cherif-Zahar, B.; Planelles, G. *J. Biol. Chem.* **2004**, *279*, 15975–15983.
- (38) Roux, B.; Bernèche, S. *Biophys. J.* **2002**, *82*, 1681–1684.
- (39) Hall, J. A.; Kustu, S. *Proc. Natl. Acad. Sci. U.S.A.* **2011**, *108*, 13270–13274.
- (40) Berezhkovskii, A.; Hummer, G. *Phys. Rev. Lett.* **2002**, *89*, 4.
- (41) Chen, H. N.; Ilan, B.; Wu, Y. J.; Zhu, F. Q.; Schulten, K.; Voth, G. A. *Biophys. J.* **2007**, *92*, 46–60.
- (42) Hummer, G.; Rasaiah, J. C.; Noworyta, J. P. *Nature* **2001**, *414*, 188–190.
- (43) Lee, Y. S.; Krauss, M. *J. Am. Chem. Soc.* **2004**, *126*, 2225–2230.
- (44) Liang, C. W.; Jansen, T. L. C.; Knoester, J. *J. Chem. Phys.* **2011**, *134*, 8.
- (45) Manca, C.; Tanner, C.; Leutwyler, S. *Int. Rev. Phys. Chem.* **2005**, *24*, 457–488.
- (46) Tanner, C.; Thut, M.; Steinlin, A.; Manca, C.; Leutwyler, S. *J. Phys. Chem. A* **2006**, *110*, 1758–1766.

- (47) Hunter, E. P. L.; Lias, S. G. *J. Phys. Chem. Ref. Data* **1998**, *27*, 413–656.
- (48) Marini, A. M.; Boeckstaens, M.; Benjelloun, F.; Chérif-Zahar, B.; André, B. *Curr. Genet.* **2006**, *49*, 364–374.
- (49) Robertson, W. H.; Diken, E. G.; Price, E. A.; Shin, J. W.; Johnson, M. A. *Science* **2003**, *299*, 1367–1372.
- (50) Elsasser, B.; Fels, G. *Phys. Chem. Chem. Phys.* **2010**, *12*, 11081–11088.
- (51) Martin-García, F.; Mendieta-Moreno, J. I.; Lopez-Vinas, E.; Gomez-Puertas, P.; Mendieta, J. *Biophys. J.* **2012**, *102*, 152–157.
- (52) Mujika, J. I.; Lopez, X.; Mulholland, A. J. *Org. Biomol. Chem.* **2012**, *10*, 1207–1218.
- (53) Riccardi, D.; Konig, P.; Prat-Resina, X.; Yu, H. B.; Elstner, M.; Frauenheim, T.; Cui, Q. *J. Am. Chem. Soc.* **2006**, *128*, 16302–16311.
- (54) Limbach, H. H.; Klein, O.; Amo, J.; Elguero, J. Z. *Phys. Chem.* **2004**, *218*, 17–50.
- (55) Smedarchina, Z.; Siebrand, W.; Fernández-Ramos, A.; Cui, Q. *J. Am. Chem. Soc.* **2003**, *125*, 243–251.
- (56) Alhambra, C.; Corchado, J. C.; Sanchez, M. L.; Gao, J. L.; Truhlar, D. G. *J. Am. Chem. Soc.* **2000**, *122*, 8197–8203.
- (57) Alhambra, C.; Sanchez, M. L.; Corchado, J.; Gao, J. L.; Truhlar, D. G. *Chem. Phys. Lett.* **2001**, *347*, 512–518.
- (58) Cui, Q.; Karplus, M. *J. Phys. Chem. B* **2003**, *107*, 1071–1078.
- (59) Jo, S.; Kim, T.; Iyer, V. G.; Im, W. *J. Comput. Chem.* **2008**, *29*, 1859–1865.
- (60) Jorgensen, W. L.; Chandrasekhar, J.; Madura, J. D.; Impey, R. W.; Klein, M. L. *J. Chem. Phys.* **1983**, *79*, 926–935.
- (61) Brooks, B. R.; Brooks, C. L.; Mackerell, A. D.; Nilsson, L.; Petrella, R. J.; Roux, B.; Won, Y.; Archontis, G.; Bartels, C.; Boresch, S.; Caffisch, A.; Caves, L.; Cui, Q.; Dinner, A. R.; Feig, M.; Fischer, S.; Gao, J.; Hodoscek, M.; Im, W.; Kuczera, K.; Lazaridis, T.; Ma, J.; Ovchinnikov, V.; Paci, E.; Pastor, R. W.; Post, C. B.; Pu, J. Z.; Schaefer, M.; Tidor, B.; Venable, R. M.; Woodcock, H. L.; Wu, X.; Yang, W.; York, D. M.; Karplus, M. *J. Comput. Chem.* **2009**, *30*, 1545–1614.
- (62) Lamoureux, G.; Harder, E.; Vorobyov, I. V.; Roux, B.; MacKerell, A. D. *Chem. Phys. Lett.* **2006**, *418*, 245–249.
- (63) Lamoureux, G.; MacKerell, A. D.; Roux, B. *J. Chem. Phys.* **2003**, *119*, 5185–5197.
- (64) Lopes, P. E. M.; Roux, B.; MacKerell, A. D. *Theor. Chem. Acc.* **2009**, *124*, 11–28.
- (65) Orabi, E. A.; Lamoureux, G. *J. Chem. Theory Comput.* **2012**, *8*, 182–193.
- (66) MacKerell, A. D.; Bashford, D.; Bellott, M.; Dunbrack, R. L.; Evanseck, J. D.; Field, M. J.; Fischer, S.; Gao, J.; Guo, H.; Ha, S.; Joseph-McCarthy, D.; Kuchnir, L.; Kuczera, K.; Lau, F. T. K.; Mattos, C.; Michnick, S.; Ngo, T.; Nguyen, D. T.; Prodhom, B.; Reiher, W. E.; Roux, B.; Schlenkrich, M.; Smith, J. C.; Stote, R.; Straub, J.; Watanabe, M.; Wiorkiewicz-Kuczera, J.; Yin, D.; Karplus, M. *J. Phys. Chem. B* **1998**, *102* (18), 3586–3616.
- (67) Kollman, P. *Chem. Rev.* **1993**, *93*, 2395–2417.
- (68) Lamoureux, G.; Roux, B. *J. Phys. Chem. B* **2006**, *110*, 3308–3322.
- (69) Laino, T.; Mohamed, F.; Laio, A.; Parrinello, M. *J. Chem. Theory Comput.* **2005**, *1*, 1176–1184.
- (70) Darve, E.; Pohorille, A. *J. Chem. Phys.* **2001**, *115*, 9169–9183.
- (71) Darve, E.; Rodriguez-Gomez, D.; Pohorille, A. *J. Chem. Phys.* **2008**, *128*, 144120.
- (72) Hénin, J.; Chipot, C. *J. Chem. Phys.* **2004**, *121*, 2904–2914.
- (73) Hénin, J.; Fiorin, G.; Chipot, C.; Klein, M. L. *J. Chem. Theory Comput.* **2010**, *6*, 35–47.
- (74) Phillips, J. C.; Braun, R.; Wang, W.; Gumbart, J.; Tajkhorshid, E.; Villa, E.; Chipot, C.; Skeel, R. D.; Kale, L.; Schulten, K. *J. Comput. Chem.* **2005**, *26*, 1781–1802.
- (75) Gao, J. L.; Xia, X. F.; George, T. F. *J. Phys. Chem.* **1993**, *97*, 9241–9247.
- (76) Flyvbjerg, H.; Petersen, H. G. *J. Chem. Phys.* **1989**, *91*, 461–466.
- (77) Bennaim, A.; Marcus, Y. *J. Chem. Phys.* **1984**, *81*, 2016–2027.
- (78) Marcus, Y. *J. Chem. Soc., Faraday Trans.* **1991**, *87*, 2995–2999.
- (79) Yu, H. B.; Whitfield, T. W.; Harder, E.; Lamoureux, G.; Vorobyov, I.; Anisimov, V. M.; MacKerell, A. D.; Roux, B. *J. Chem. Theory Comput.* **2010**, *6*, 774–786.

NOTE ADDED AFTER ASAP PUBLICATION

A partially corrected version of this paper was posted ASAP June 12, 2012. Additional corrections have been made and the corrected version was reposted June 13, 2012.